Functional Imaging of the Vascular Bed by Dynamic Optical Tomography

Randall L. Barbour,[1a] Harry L. Graber,[1a] Yaling Pei,[2] Christoph H. Schmitz,[1a] Yong Xu,[1a] Adriana Di Martino,[3] F. Xavier Castellanos,[3] David P. Klemer,[1a] Rosemarie E. Hardin,[1b] Nelson A. Franco,[1b] Michael S. Katz,[1b] Michael E. Zenilman,[1b] Alessandro G. Smeraldi,[4] and Thomas F. Panetta[4]

1. Departments of [a]Pathology and [b]Surgery, SUNY Downstate Medical Center, 450 Clarkson Avenue, Brooklyn, NY 11203
2. NIRx Medical Technologies, LLC., 15 Cherry Lane, PO Box 134, Glen Head, NY 11545
3. NYU Child Study Center, 577 First Avenue, New York, NY 10016
4. Department of Vascular Surgery, Staten Island University Hospital, Staten Island, NY 10305

Abstract

In this report we present a brief outline of our technological approaches to developing a comprehensive imaging platform suitable for the investigation of the dynamics of the hemoglobin signal in large tissue structures using NIRS imaging techniques. Our approach includes a combined hardware and software development effort that provides for i) hardware integration, ii) system calibration, iii) data integrity checks, iv) image recovery, v) image enhancement and vi) signal processing. Presented are representative results obtained from human subjects that explore the sensitivity and other capabilities of the measuring system to detect focal hemodynamic responses in the head, breast and limb of volunteers. Results obtained support the contention that time-series NIRS imaging is a powerful and sensitive technique for exploring the hemodynamics of healthy and diseased tissues.

1. Introduction

Near infrared spectroscopy (NIRS) is increasingly being employed as a noninvasive monitoring tool for the investigation of functional states of tissue. Favoring this development is its ability to probe deep tissue structures at wavelengths and intensities that are non-damaging, while employing instrumentation that is economical and portable. Beginning in the late nineteen eighties, our group first recognized that by employing array sensing techniques in combination with image reconstruction methods based on physical models of light scattering, the NIRS method could be extended to provide for 3D images of optical contrast features of tissue.[1,2,3] Since these early reports, interest in diffuse optical tomography (DOT) has grown steadily to encompass a broad spectrum of investigations and technology development efforts.[4,5]

From its earliest inception, DOT was envisioned as a method that could be used to obtain estimates of absolute tissue optical properties.[3,6,7] Experience has shown that this approach is fraught with technical difficulties,[8,9] and instead the method appears more suitable to measures of relative changes in optical properties.[10,11,12] Recognition of this has prompted our group to develop instrumentation suitable to explore the temporal dynamics of tissue attributable mainly to naturally occurring or induced fluctuations in the hemoglobin signal.[13,14] In this report we provide an updated description of our technology development efforts and give examples of results from clinical studies that support the growing evidence of the broad based utility of DOT technology to explore relevant functional states and disease processes.

2. DOT Technology

Central to our instrumentation development efforts is the capacity to capture a time series of images. From the outset we have recognized the need to go beyond the obvious aim of simply developing a suitable data collection device. Instead, we have sought to tackle the much larger problem of implementing a full spectrum of tools that are necessary to extract useful metrics from dynamic studies. To this end our development efforts have concentrated about six principal tasks: i) hardware integration, ii) system calibration, iii) data integrity, iv) image recovery, v) image enhancement and vi) signal processing.

2.1. Hardware Integration: Guiding our approach to developing a suitable tomographic system has been a consideration of conflicting demands between hardware performance, expected limits of image recovery algorithms, and the response characteristics of the vascular bed. To explore the third of these in any meaningful detail it is necessary to sample temporal states on a time scale sufficiently fast to capture the relevant features. For most studies this means acquiring tomographic data at an image framing rate of at least 3 Hz. Because most studies will require signal acquisition from multiple source positions, it is necessary to implement either a fast optical switch (in the case of a time-multiplexing scheme) or a frequency encoding scheme which provides for simultaneous multi-site illumination.[15] We have chosen the former to provide for a more dense sampling of the emerging light field (important for image recovery). We have complemented this approach by also introducing a gain switching scheme that allows for signal capture over a very large dynamic range (10^9) together with use of sample-and-hold circuitry to provide for parallel data capture. In practice we have implemented a hybrid illumination scheme wherein time multiplexing of the source is combined with frequency encoding techniques to allow for discrimination of different illuminating wavelengths (necessary for spectroscopic studies) delivered simultaneously at any one site. The resulting design provides for an image framing rate that is variable, between 2 and 90 Hz, depending on the number of source positions employed per image scan. Our design is also easily scalable to allow for the capture of greater source-detector densities beyond our typical 32×32 configuration, should the need arise.

In Figure 1 we show a functional layout of our imager with expanded views of the instrument set-up and real-time data display screens. Depicted is a four-level functionality scheme comprising system hardware, system control, data analysis and image display. The basic system provides for frequency encoding of up to four laser diodes, a fast optical switch with incoupling optics, use of various measuring heads, a multichannel parallel detector module equipped with adjustable gain control, and a system controller.

2.2. System Calibration: A critical functionality of any measuring system is the availability of a robust calibration scheme. In the case of DOT technology, a nontrivial challenge is the expectation that most measurements of interest will involve data sampling with a large number of source-detector channels ($\sim 10^3$). Our approach has been to devise a scheme wherein expected differences in light delivery and collection among the channels can be defined under the same conditions as the experiment.[13] This is an important consideration for routine system monitoring. In addition, we have sought to provide for such monitoring in ways that readily permit generation of statistical estimates of critical performance parameters. The scheme we have developed makes use of expected symmetry from laboratory phantom vessels. In this way deviations from symmetry are used to compute coefficients that account for differences in light transmission among the light delivery and receiving optics. We should note that this approach, which is essentially a data driven scheme, differs from a recent report[16] that considers system calibration based on predictions using physical models of light propagation in scattering media.

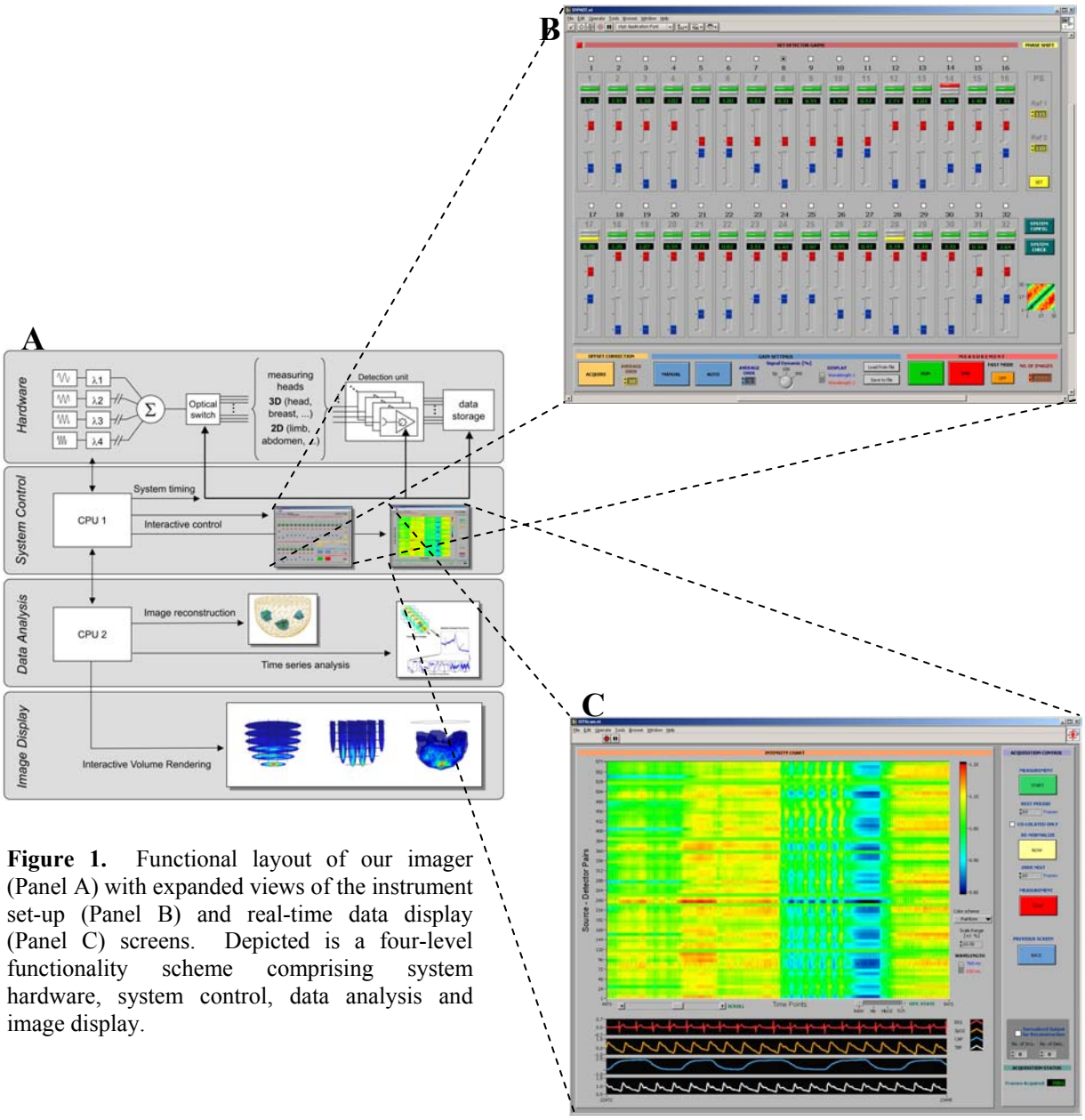

Figure 1. Functional layout of our imager (Panel A) with expanded views of the instrument set-up (Panel B) and real-time data display (Panel C) screens. Depicted is a four-level functionality scheme comprising system hardware, system control, data analysis and image display.

2.3. Data Integrity: Ensuring data integrity is of fundamental importance in any physical measurement. The challenge for time-series DOT studies is to devise schemes that are appropriate to handle the volume of data collected from the many thousands of data channels. We have treated this problem as comprising three components. The first is basically an issue of optimizing alignment of the optical transmission paths. To facilitate this we have implemented various computer-assisted real-time visualization routines that serve to augment alignment of the incoupling optics as well as align light delivery through the optical switch to the source fibers. The second concerns monitoring for stray noise from various causes that can compromise data quality. Here we have implemented dark noise and optical phantom checks that serve to measure levels of noise, as a function of gain setting, that are attributable to system electronics, optical incoupling, and other factors. The third data integrity check deals with obtaining an objective measure of the fidelity of optode contact at the tissue surface. Here we have taken advantage of the physical principle known as

reciprocity.[17] This holds that light entering a scattering medium at one point and exiting at another will provide the same signal strength should the positions of the source and receiver be reversed. In practice this is accomplished using a nested, or coaxial, fiber design with light delivery fibers located in the center of the fiber bundle surrounded by halo of light collecting fibers. Using this approach, a comparison of reciprocal channels can immediately identify coupling differences and allow for optode repositioning prior to data collection.

2.4. Image Recovery: The image recovery scheme that we first considered made use of a linear perturbation model.[2,3] As typically viewed, this approach seeks to define the absolute optical properties of a scattering medium. While conceptually possible, this goal if fraught with technical difficulties in defining with sufficient accuracy the boundary conditions that coincide with those of measurement. Several years ago, Pei described an image recovery scheme that can evaluate relative changes in the optical properties of a scattering medium.[11,18] A key element of this algorithm, which is referred to as the Normalized Difference Method (NDM), was the demonstration that the resulting scheme is remarkably robust to the image degrading effects of systematic mismatches in the boundary conditions. This scheme has proven pivotal in our efforts to develop a practical time-series imaging capability. The key issue here is basically a practical one. Whereas efforts to recover absolute coefficients can work, they often require use of recursive iterative schemes that are computationally expensive.[19] In contrast, we have shown that the same uncertainties that require the need for these intensive computations have much less impact on image quality using the NDM scheme. Because of this, we believe that much of the relevant dynamics attributable to vascular dynamics can be reliably explored using computationally efficient solvers such as the truncated SVD method.

Before leaving this topic, we wish to make one more point. While an explanation accounting for why the NDM scheme can provide improved image results with minimal computational effort was given in Ref. 11, its significance has been largely overlooked. Without belaboring the point, we simply point out that linear perturbation theory holds that the information content of the data vector, ΔI, (i.e., difference between measured and predicted light field intensities) is in some way proportional to the light field distributions produced by the true underlying optical properties of a medium. We showed that, in practice, the former can be severely corrupted by even modest errors in specifying the boundary conditions. This finding suggests that the underlying sensitivity of absolute reconstruction schemes is an inescapable consequence of the physics of light transport in scattering media. We have interpreted this to suggest that system calibration and data processing schemes focused on the absolute image recovery problem will prove a far more daunting challenge that those that consider measurements based on relative changes.

2.5. Image Enhancement: Image quality is often the key factor that determines the practicality of an imaging scheme. Experience with DOT has indicated that images of only modest spatial resolution are thus far possible.[20] Recently we have pursued a development effort intended to improve achievable image resolution using a correction scheme motivated by consideration of the most commonly used method of acquiring magnetic resonance imaging (MRI) data. The essence of MRI is the notion of frequency encoding of spatial information. In the case of MRI, this is accomplished by imposing a gradient in the magnetic field across the target to be imaged. The effect of this is to allow for discrimination between signals originating from one position in space and from another, because each is associated with a different resonance frequency. Viewed alternatively, this approach allows for an unambiguous mapping of frequency-encoded information from the object domain into the image domain.

We have recognized that this approach can be extended to the case of time-series DOT imaging. The idea is to somehow identify how information in the object domain is mapped to the image domain. As in the case of MRI, we have reasoned that if each pixel in the object space were somehow encoded with a different frequency, then an examination of the Fourier spectrum of each pixel, computed from a time-series of reconstructed images, should identify precisely where and by how much the true information is

being mapped. Note that our consideration here is a mathematical one, and not physical. The goal is to define, as precisely as possible, just how a particular reconstruction algorithm maps information into the image domain. It should be noted that such details are largely unknown for most algorithms. We have since recognized that the scheme, outlined subsequently, is conceptually similar to the established practice

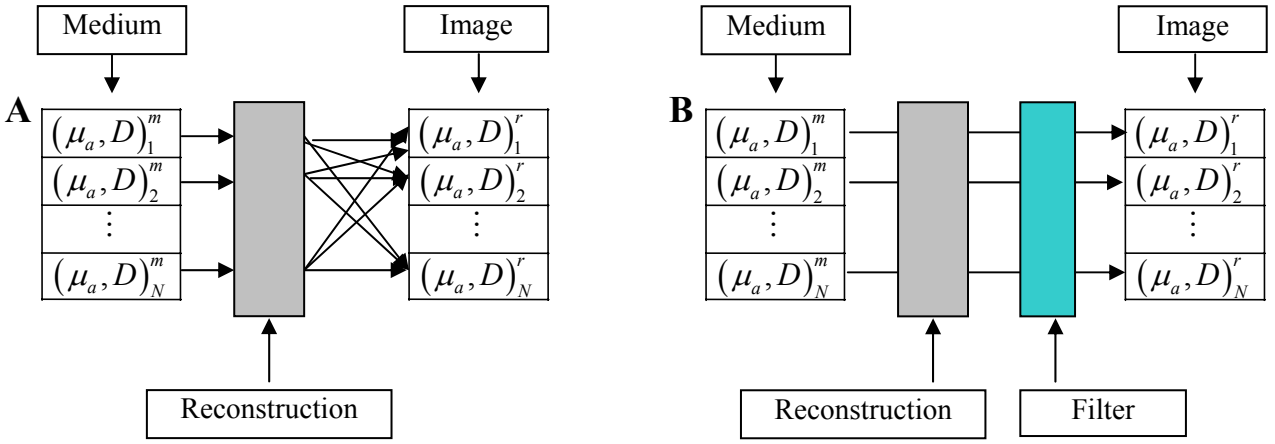

Figure 2. Panel A, schematic depicting the action of typical DOT image reconstruction algorithm, which yields blurred images because information from each object domain location is mapped to more than one position in the image domain. Panel B, the action of an ideal image-correcting filter, which is to counteract the information spreading aspect of the reconstruction algorithm's action.

of correcting images based on knowledge of a measuring system's point spread function (PSF). Because we are considering a computational problem, we have adopted the term information spread function (ISP). An illustration depicting this scheme is shown in Figure 2. Panel A shows that most image recovery algorithms, especially in the case of DOT, yield blurred images because localized information from the object domain is mapped to more than one position in the image domain. The goal is to implement an image filtering scheme that corrects for these inaccuracies, producing, as depicted in Panel B, a final image that comes as close as possible to a one-to-one correspondence between object and image pixels.[21] To derive the mathematical operator designated "Filter" in Fig. 2(B), we begin by assigning a distinct type of temporal variability to the optical parameters of each volume element of a target medium. By numbering the volume elements in a consistent manner, every state of the medium can be completely described by a vector $\mathbf{x}_0^{(i)}(\mathbf{r}) = [x_{01}^{(i)} \;\; x_{02}^{(i)} \;\; \ldots \; x_{0M}^{(i)}]^{\mathrm{T}}$, $i = 1, 2, ..., N$. Here, i is the time, or state, index, M is the number of volume elements, and N is the number of time steps considered in the filter computation. (As a practical matter, $N \gg M$ gives best results.) A set of detector data for the spatial distribution of material properties represented by $\mathbf{x}_0^{(i)}(\mathbf{r})$ is computed (i.e., forward problem), and then the corresponding image $\mathbf{x}_r^{(i)}(\mathbf{r})$ is reconstructed. Repeating these operations for all N time steps yields the corresponding $M \times N$ matrices $\mathbf{X}_0^N(\mathbf{r})$ and $\mathbf{X}_r^N(\mathbf{r})$, where $\mathbf{X}_0^N(\mathbf{r}) = [\mathbf{x}_0^1(\mathbf{r}) \;\; \mathbf{x}_0^2(\mathbf{r}) \;\; \ldots \; \mathbf{x}_0^N(\mathbf{r})]$ and $\mathbf{X}_r^N(\mathbf{r}) = [\mathbf{x}_r^1(\mathbf{r}) \;\; \mathbf{x}_r^2(\mathbf{r}) \;\; \ldots \; \mathbf{x}_r^N(\mathbf{r})]$. Finally, the $M \times M$ filter matrix $\mathbf{F}$ is obtained by solving the linear system $\mathbf{X}_0^N(\mathbf{r}) = \mathbf{F}\mathbf{X}_r^N(\mathbf{r})$. Subsequently, any image $\mathbf{y}_r$ that is reconstructed using the same volume element pattern and measurement geometry as used in the computation of $\mathbf{F}$ is corrected by calculating the matrix product $\mathbf{F}\mathbf{y}_r$.

Shown in Figure 3 is an example of the image enhancement capability that can be achieved using the temporal encoding scheme outlined here. For demonstration purposes it is preferable to work with a medium whose optical parameters are known, so that the accuracy of the reconstructed images may be quantified. Consequently, the target "tissue" used here was a simulated hemispherical structure containing three small absorbing spherical regions embedded in a more weakly absorbing homogeneous background. Proceeding from left to right in Fig. 3 are 2D projections of the original, unfiltered reconstructed and

filtered reconstructed images, respectively, of the 3D target medium. Comparison shows that use of the filtering technique can significantly improve image quality.

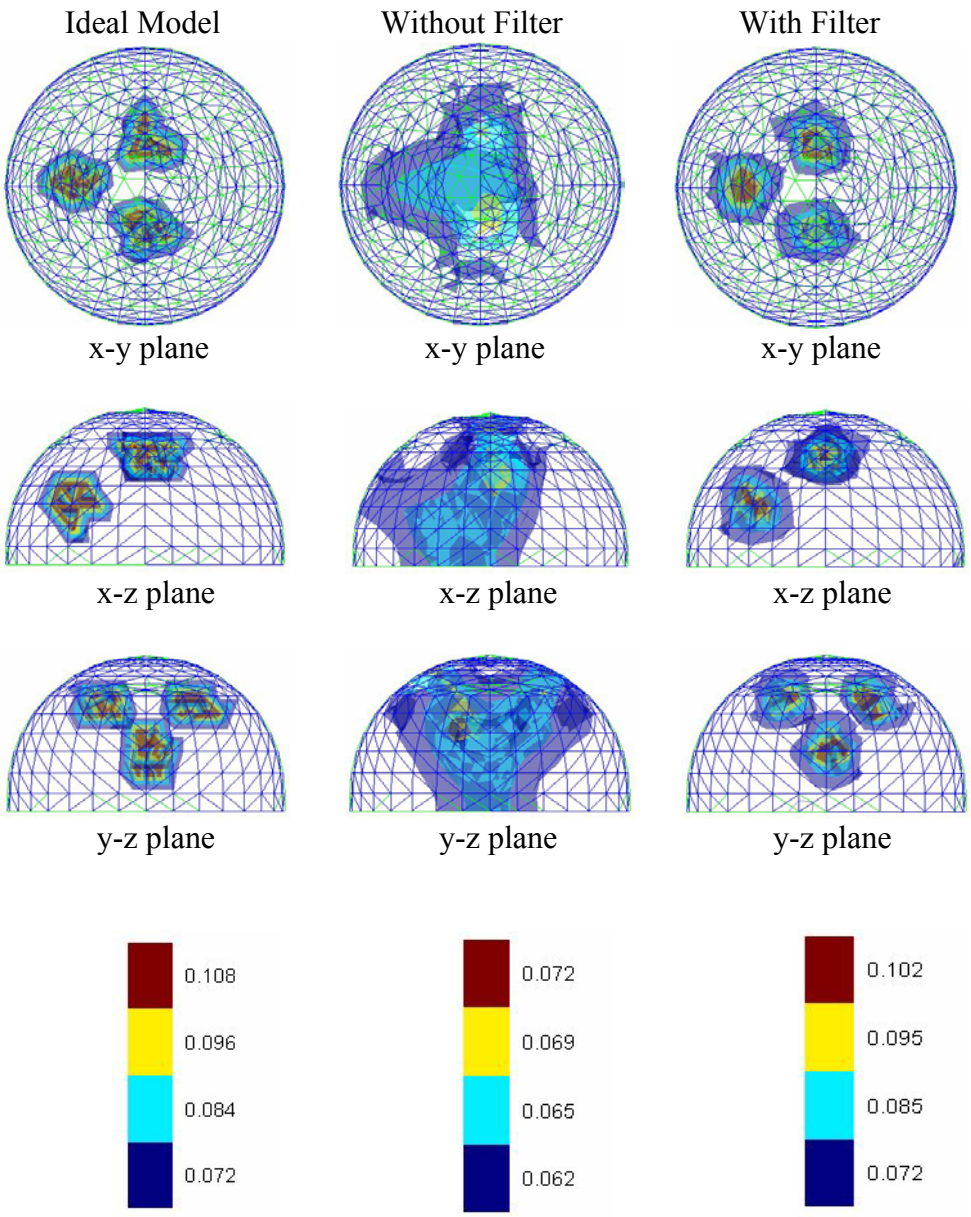

Figure 3. Target and reconstructed images of absorption coefficient from simulated data for the case of the hemisphere geometry with three inclusions. The first column is the target from different views, the second is the reconstructed images without filter correction, and the third is the results with filter correction. In which the background scattering and absorption coefficients are, respectively, $\mu_s' = 10$ cm^{-1} and $\mu_a = 0.06$ cm^{-1}. The absorption coefficients in the inclusions are all $\mu_a = 0.12$ cm^{-1}, while their scattering coefficients are the same as that of the background.

2.6. Signal Processing: While the preceding capabilities provide for the collection and recovery of an image time series, this information by itself is not in the form that many would find particularly useful. The challenge here is the need to explore the four-dimensional image "spacetime" and related data in ways that provide for the separation and characterization of information from a complex composite. Considerations here are both mathematical and physiological. The latter includes the phenomenology of the vascular tree and its architecture. Arteries, veins and microvessels are omnipresent in biological tissues. In addition, each of these elements is modulated by different natural mechanisms, resulting in distinct dynamics. Thus, for instance, the arterial tree is dominated by a cardiac beat frequency caused by ventricular contraction. The venous tree exhibits a respiratory frequency caused by rhythmic compression of the inferior vena cava due to movement of the diaphragm, and by concomitant rhythmic variations in thoracic pressure. The microvessels undergo oscillations in diameter in response to variations in sympathetic tone, actions of circulating hormones (e.g., angiotensin), and local metabolic factors (e.g., nitric oxide). In addition to these naturally occurring dynamics, there are many instances wherein the study of induced dynamics is useful. Note that time-series DOT studies offer more than the ability to non-invasively explore states of vascular dynamics. Recall that hemoglobin, which is the principal chromophore affecting the dynamics of near infrared light transmission in tissue, is also the principal species responsible for oxygen transport to tissue. Thus time-series DOT also allows for the investigation of factors that influence the interaction between tissue and its blood supply (i.e., tissue-vascular coupling).

These considerations reinforce the observation that the architecture of the vascular tree and its modulation produce a state such that light passing through tissue anywhere will contain information that has both local and systemic origins. In many instances, it is important to separate these signals, which leads us our the next consideration—the spectrum of numerical methods that are suitable for such investigations.

The field of signal processing is a broad subject encompassing a large number of analysis techniques. In our examination of time-series DOT we find it useful to restrict our consideration to four principal areas: time-frequency, time-correlation, rate analysis and signal separation. To this end we have implemented in Matlab a pull-down-menu driven toolbox that provides for these and other operations.[22] Our interest in time-frequency methods stems for the expectation that many physiological processes are nonstationary,[23] exhibiting a temporally varying frequency structure. The correlation methods are useful in exploring expected relationships among data, especially in cases where time delays can occur. Rate analysis, as the name implies, allows for the determination of how fast responses occur, usually in response to a provocation. Of particular interest in many instances are the use of signal separation techniques, which generally speaking represent a class of multivariate statistical methods. Two sub-categories that we have found particularly useful are blind source separation techniques, for cases where prior knowledge of the system dynamics is not at hand, and strongly model-based methods, for cases where one seeks to locate and quantify specific forms of known behavior in a target tissue.[24] The former are exemplified by principal component analysis (PCA) and by PCA plus extended temporal decomposition[25]; the second of these yields distinct forms of behavior that are maximally independent.[26] The latter are exemplified by general linear model (GLM) computations,[25] which gives quantitative estimates of the probability that a particular type of temporal fluctuation (i.e., a model function) is present in each image pixel, and the percentage of the total temporal variance that a model function explains or accounts for in each pixel.

3. Methods

All experimental data reported on below were collected using a DYNOT system (NIRx Medical Technologies LLC., Glen Head, NY) for dynamic DOT. Depending on the particular application, the number of optical fibers used for light delivery and recording was $N = 24$, 30, or 62. In all cases the sampling rate was approximately 2.5 complete data sets per second. As outlined above (§2.1), measurements were performed at two wavelengths simultaneously. All measurement data were subjected

to the reciprocity-based data integrity checks referred to in §2.3,[27] and data from any channel pairs that failed to show the expected degree of reciprocity were excluded from subsequent analyses. Individual data channels also can be rejected if they saturate during any part of the measurement, or if the coefficient of variation of intensity values recorded during a resting baseline period exceeds a preset threshold.

All reported images were reconstructed by solving a linear perturbation equation, modified in accordance with the NDM (§2.4). Solutions of the resulting linear systems were computed by using a truncated SVD algorithm.[28] For the demonstration of the image-correcting power of the temporal encoding technique (§2.5), the numbers of image pixels and filter-generating time steps were $M = 982$ and $N = 16384$ (i.e., 2^{14}), respectively; a LU decomposition algorithm was used to solve the linear system $\mathbf{X}_0^N(\mathbf{r}) = \mathbf{F}\mathbf{X}_r^N(\mathbf{r})$. The signal-separation computations (§2.6) that were performed on selected detector and image time series were carried out in the manner described in Ref. 25.

4. Results

4.1 Functional Neuroimaging. Focal neuronal activation is expected to produce an event-related increase in blood flow, causing an increase in blood volume with improved oxygenation.[29,30] An example of our ability to record such responses from the head of an adult (motor cortex) in response to a box-car finger-tapping paradigm is shown in Figure 4. Illustrated is an event-related change in oxy-Hb levels paralleling the onset and cessation of finger tapping. Shown in Figure 5 are results from a similar experiment in which collected data were further processed to yield a spatial image of the response. Here we show the result obtained when the GLM technique was applied, with the boxcar design as the model function, to identify where in the image space this particular behavior was present. It is seen that the boxcar makes a significant contribution to the overall model fit in only a single, highly localized, region that is located approximately 0.5-1.0

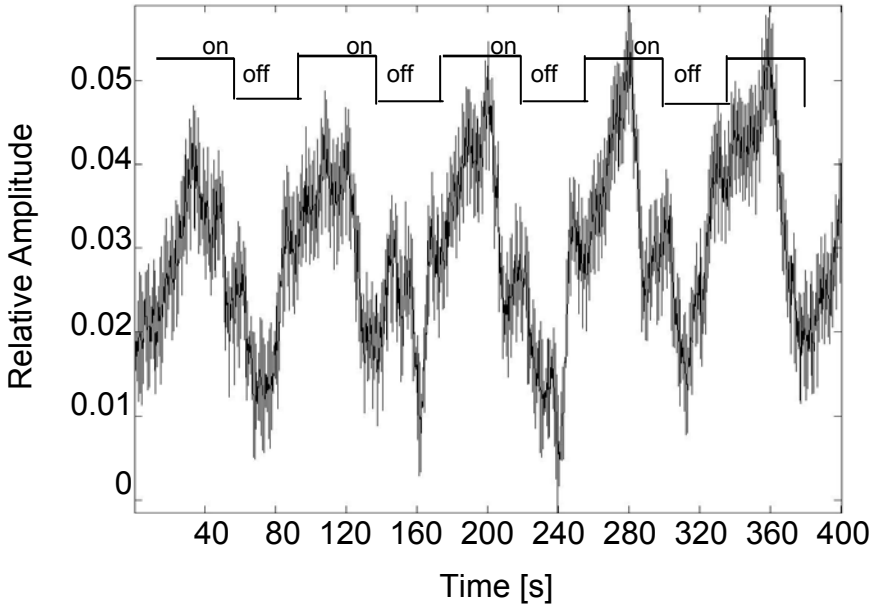

Figure 4. Temporal response of the oxy-Hb signal (first principal component) during finger-tapping sequence.

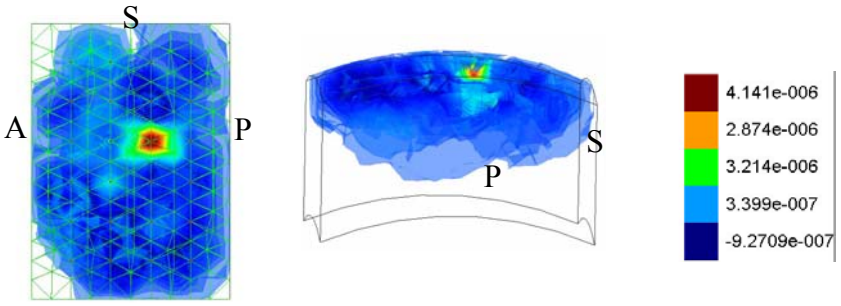

(a) (b)

Figure 5. Each image is a spatial map of the coefficient for the GLM fit of the boxcar model function to the pixels' oxy-Hb time series. Two views are shown for the activation-rest time period. The *t*-statistics associated with largest positive and largest negative values of the GLM best-fit parameter are +9.25 ($p = 3.6\times10^{-19}$) and -7.09 ($p = 3.6\times10^{-12}$), respectively. A = anterior P = posterior, S = superior.

cm below the surface, a finding is consistent with results from fMRI studies.

4.2. Optical Mammography

4.2.1. Breast Cancer Detection by Transient Induced Hypoxemia. The detection of focal hemodynamic responses has applications to other studies. Here we have explored our ability to detect a solid tumor of the breast by subjecting the tumor to a period of transient hypoxemia, via a simple breath hold. The rationale for this maneuver was that the enhanced metabolic activity associated with a growing tumor, combined with a possibly compromised vascular supply, could push the tumor tissue into oxygen debt, which would cause a decline in the level of oxy-Hb together with a rise in the level of deoxy-Hb.[31] In Figure 6 we show a typical time course in the measured normalized levels of oxy-Hb and deoxy-Hb obtained before (1 and 2), during (3) and after (4) the breath hold, for the healthy and tumor-bearing breasts. Comparison between the graphs reveals a qualitatively different trend in hemoglobin states during

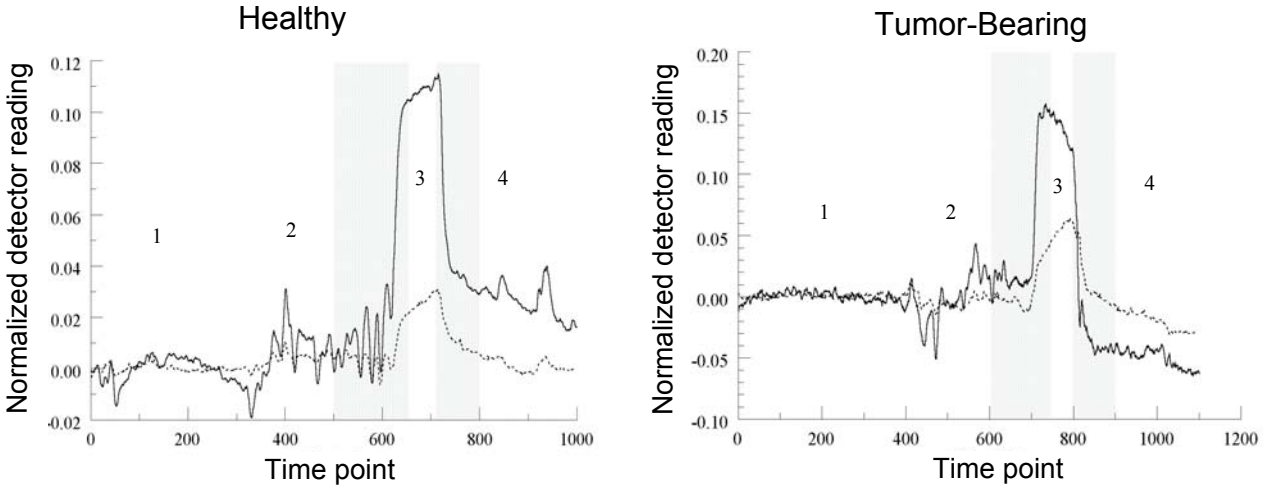

Figure 6. oxy-Hb (solid line) and deoxy-Hb (dotted line) time series computed from representative (non-simultaneous) dual-wavelength detector readings.

the breath hold. In both graphs, the oxy-Hb and deoxy-Hb levels rose initially upon a breath hold, which is the expected response because the associated rise in venous return pressure will cause an increase in tissue blood volume. Following this, in contrast to the trend seen in the healthy breast, the oxy-Hb level in the tumor-bearing breast became unstable and then declined. At the same time, the deoxy-Hb level climbed more rapidly than in the breast that did not contain a tumor. These findings are entirely consistent with the well-recognized general finding that solid tumors function on the brink of hypoxemia.

In Figure 7 we show an example of how information of the sort in Fig. 6, but extracted from the image time series reconstructed from the tomographic measurements, can serve to image the tumor with high contrast. The data-analysis protocol was: 1) subject held her breath for approximately one minute; 2) simultaneous dual-wavelength measurements were performed at a rate of ~3 Hz during this time; 3) time series of absorption coefficient (μ_a) images, at both wavelengths, were reconstructed; 4) time series of spatial maps of oxy-Hb and deoxy-Hb were computed from the μ_a images for each time point; 5) linear regression computations were performed to determine the average rate of change of oxy-Hb and deoxy-Hb in each image pixel, within time period 3 (narrow white bar within the gray bar) indicated in Fig. 6; 6) a spatial map of the product of the oxy-Hb and deoxy-Hb regression slopes was generated. For presentation clarity, we show only those contour levels that comprise the highest 90% of the computed values (i.e., background contrast is <10% of the maximum value shown. Comparison of this result to the sonogram image of the same breast indicates excellent agreement. The equivalent result obtained from the normal breast (not

shown) yielded a spatial map that was essentially featureless within the contrast ranges shown. These findings thus show that known disturbances in the vascular biology of solid tumors can be accurately localized from analysis of an image time series of the hemoglobin signal.

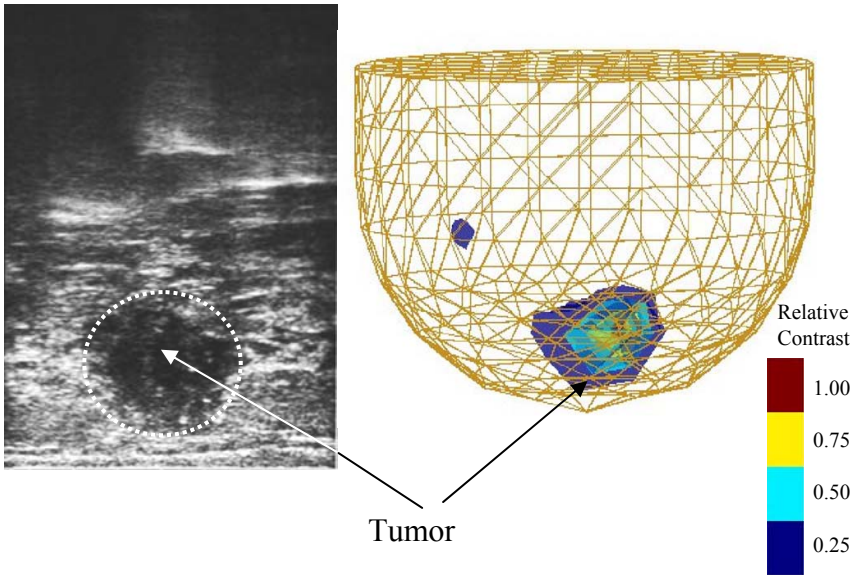

Figure 7. Right, 3D DYNOT image of tumor identifying imbalance in tissue oxygen supply/demand. Image was produced without need of contrast agents or compression. Left, sonogram image of same breast showing location of tumor. Note close agreement in size and shape.

4.2.2 Simultaneous Dual Breast Measurement:

The hemodynamic disturbances of the sort shown in Figures 6 and 7 suggest that enhanced detection capability might be realized from a simultaneous bilateral measurement. The rationale here is that provocations having a central origin, (e.g., a respiratory maneuver) will simultaneously influence both breasts, allowing for a perfectly time-correlated comparison. A photograph of the measuring head used in these studies is shown in Figure 8. Illustrated are two cup-shaped devices composed of black Delrin, designed to accommodate up to a "C" size breast. Each cup can be fitted with up to 62 source-detector fibers whose position are pneumat-ically adjustable under computer control. In Figure 9 we show an example of the parallel response obtained using this device, recorded from a healthy volunteer in response to a Valsalva maneuver. Indicated are the relative changes seen in the average oxy-Hb, deoxy-Hb and total Hb signals computed from the measurement array (12 sources, 15 detectors for each breast). Inspection reveals that the vascular reactivity of blood vessels to the maneuver are highly coordinated in both breasts, which is the expected response for a healthy individual.

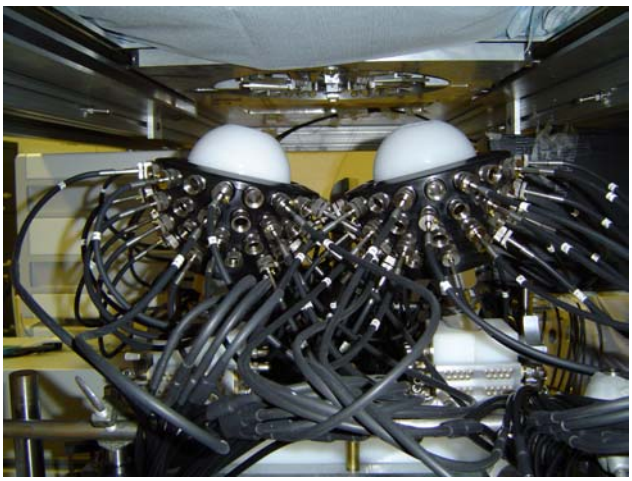

Figure 8. Photograph of measuring head used for simultaneous dual-breast measurements. Thirty-one source-detector fibers are distributed over the surface of each breast.

Recently we have repeated this protocol on two other subjects. One was a healthy control, and the other a patient diagnosed with bilateral breast cancer. The mean Hb time series for the former (healthy control) subject are qualitatively and quantitatively similar to those in Fig. 9. In contrast, the latter subject (cancer patient) yielded responses that were significantly distorted compared to the healthy subjects and with less similarity between the left- and right-breasts. Most evident was the finding that the peak amplitude of the Hb deflections was reduced compared to control subjects, by a factor of ~6. This finding is consistent with

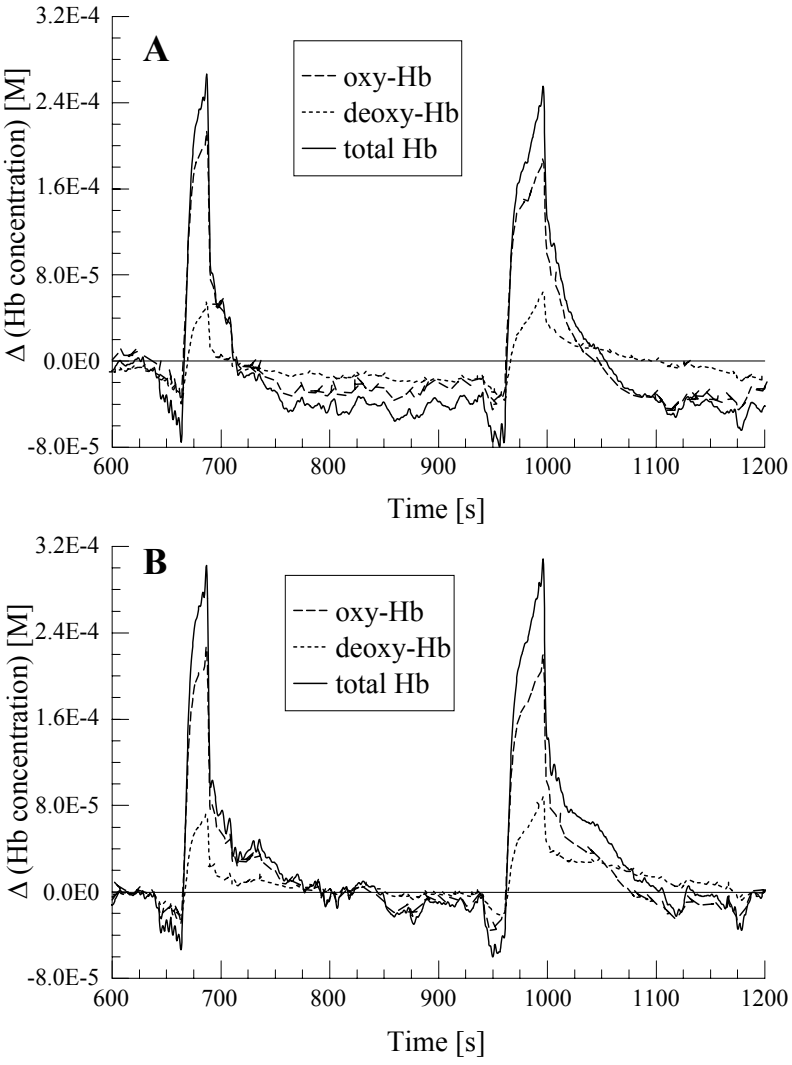

Figure 9. Average concentration change (relative to baseline average value) for the separate hemoglobin states and for total Hb, for the left (Panel A) and right (Panel B) breasts of a healthy control subject in an optical mammography study. Following a 10-minute baseline period (not shown), a sequence of quantitative Valsalva maneuvers was performed at intervals of ~5 minutes.

the known increase in tissue oncotic pressure that typically occurs in tissue structures containing solid tumors. This increase, resulting from leakage of fluid from incompetent tumor blood vessels into the interstitial space, substantially limits the ability of veins in the affected tissues to distend during maneuvers that produce increases in intrathoracic pressure.

4.3 Imaging of Peripheral Hemodynamics: There are other forms of hemodynamic responses that can be explored from analysis of time-series image data. One having particular relevance to management of many disease states are measures of peripheral vascular resistance. For instance, we have postulated that the application of mild venous occlusion (60 mm Hg), for example to the upper arm, might be sufficient to cause distension of the distal vascular bed and that the magnitude and dynamics of this response would correlate with vascular resistance. We further postulated that factors that affect the latter will impact on the former in a quantifiable manner. To examine this we performed a time-series study on the forearm of a volunteer. The imaging system employs a pneumatically controlled measuring head consisting of 24 source and 24 detector fibers uniformly spaced in a circular array.[32] Data collection was accomplished by fitting the device to a point on the forearm approximately one-third the distance between the wrist and elbow. Also attached was a pneumatic cuff applied to the upper arm, and a heating pad surrounding the forearm, proximal to the measuring site. Shown in Figure 10 is the time course of oxy-Hb levels averaged over all measuring sites (24 sources, 24 detectors) with and without application of external heat, in response to replicate cycles of mild venous occlusion. Inspection shows that inflation of the cuff results in marked rise in the level of oxy-Hb, which indicates distal pooling of blood. More important, we see that the magnitude and dynamics of this response is enhanced by application of heat (light curve), which we interpret as a result of a local decrease in peripheral vascular resistance.

To reinforce this suggestion, it is instructive to ask where in a two-dimensional cross sectional spatial map of the forearm behavior of the type illustrate in Fig 10 might be found. One approach is to compute a cross-

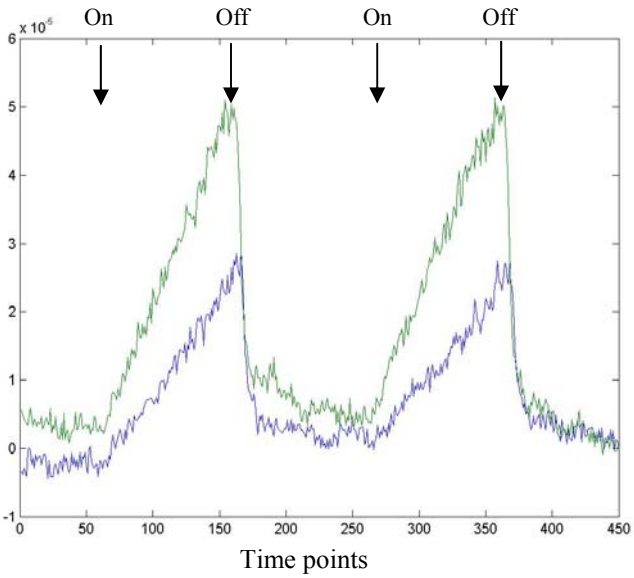

Figure 10. Time course of computed average oxyhemoglobin response to two cycles of mild venous occlusion in the forearm. Dark curve, no heat applied; light curve, with heat.

correlation (CC) map between one of the functions plotted in Fig. 10 and an image time series reconstructed from optical tomographic data. Regions where the behavior dominates will have a high positive correlations. An example of this is shown in Figure 11. For comparison purposes we also provide a MR map (Panel A) taken from the same location as that where the optical measures were performed. It is seen that most of the image (Panel B) is strongly correlated with the imposed venous modulation. Shown in Panel C is plot of the of the correlation value as a function of time delay in this region. We see that the dependence persists, indicating that the response is predominantly coherent. Shown in Panel D is a similar plot for a region of significantly reduced correlation. Interestingly, as seen in Panel E, this region and the adjacent area to the upper right overlay the radius and ulna, suggesting that interosseous hemodynamics differs from that of surrounding tissue, as of course it does.

4.3.1 Image Analysis via Signal Separation Techniques: The experiment reported on here permits us to demonstrate still additional capabilities of dynamic DOT. For instance, it is clear that the overall vascular response is a composite of multiple phenomenologies. At an elementary level this is evidenced by the different natural beat frequencies associated with the principal elements of the vascular tree, as discussed above (see §2.6). It is our view that characterization of the oscillatory behavior of microvessels, in particular, with a real-time imaging modality can provide a wealth of functional indicators that will prove helpful in clinical diagnosis and management. These indicators will be derived from the detailed knowledge of peripheral hemodynamics that dynamic DOT can provide. An example of this is shown subsequently. Given the known complexity of vascular dynamics, it should be useful to employ signal processing techniques that are capable of extracting measures into physiologically meaningful components. To accomplish this we have, as stated above (§2.6), employed several blind source separation techniques. Results shown in Figure 12 are an example of use of PCA applied to the experimental data illustrated in Fig. 11. Plotted here are the first two principal components computed from the reconstructed image time series for oxy-Hb in the case of four consecutive mild inflation cycles. The dark curve corresponds to the 1st principal component (PC) and accounts for approximately 80% of the total signal variance. The light curve is the 2nd PC and accounts for approximately 10% of the variance. (Note that the plotted functions have been normalized to unit Euclidean length (unit sum-of-squares).) Careful inspection reveals that the dynamics of the two functions differ, and that they change from one application of mild venous occlusion to the next. In the case of the 1st PC, we see that it corresponds to oxy-Hb levels increasing almost immediately upon cuff inflation. It is also seen that the magnitude of this response increases modestly following the second challenge. We interpret this component to represent blood volume changes occurring in the venous tree, as it is these structures that distend most easily when blood pressure increases. The findings associated with the second PC are more complex. Early on in the inflation cycle, this component corresponds to an initial *decline* in oxy-Hb level followed by a accelerated increase relative to the 1st PC, and that the magnitude of the latter increases markedly in subsequent cuff challenges. We believe this signal originates primarily from the microvascular bed. The initial decline in oxy-Hb is consistent with blood pooling allowing for greater oxygen extraction. Following this, dilation occurs, perhaps in response

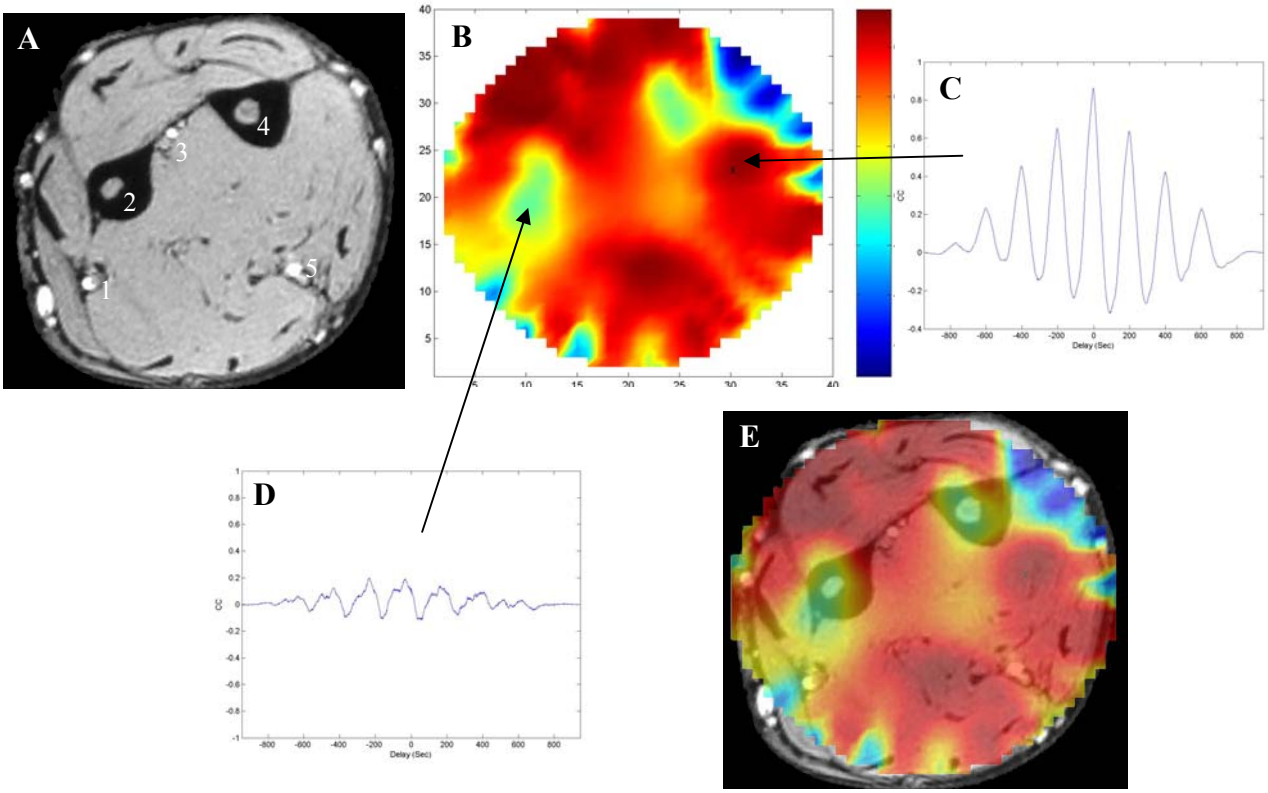

Figure 11. Panel A, MR cross section of arm. Panel B, cross correlation (CC) map between (dark) model function in Figure 10 with Hb image time series. Panel C, overlay of Panel A and B. Panels D and E, time dependence of CC at indicated locations. (1) Radial artery, (2) radius, (3) interosseous artery, (4) ulna, (5) ulnar artery.

to the buildup of local metabolic factors. The finding that the rate and extent of change in this signal increases in subsequent challenges suggests that insufficient time had elapsed between cycles to allow for complete washout of the tissue factors. Additional support of these interpretations can be found in Figure 13, which shows spatial maps of the amplitude of the 1st and 2nd PCs. In Panel A we see that the signal associated with the 1st PC is seen mainly in the periphery (red regions), roughly in agreement with the location of near-surface veins (see Panel 11A). In contrast, the signal associated with the 2nd PC is found mainly in the ventral aspect of the forearm, which is dominated by well-perfused muscle. These findings reinforce results from the other studies demonstrating that time-series DOT can define focal changes in vascular hemodynamics.

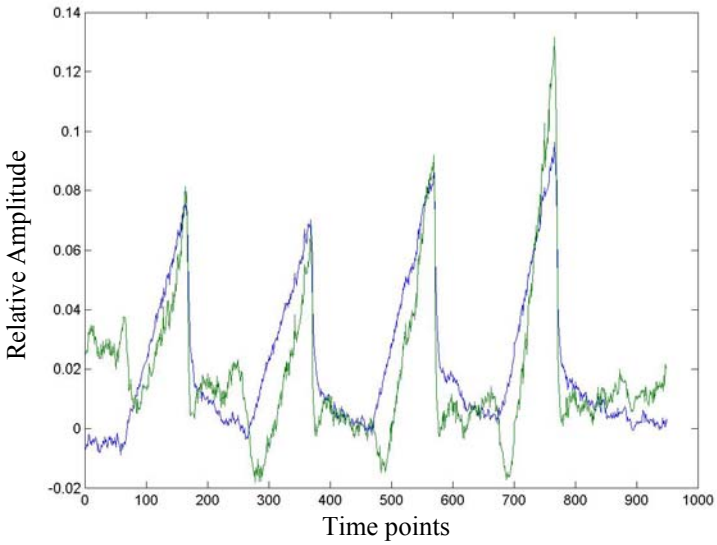

Figure 12. 1st (light curve) and 2nd (dark curve) PC of oxyhemoglobin signal computed for reconstructed image time series for four consecutive cuff inflation cycles.

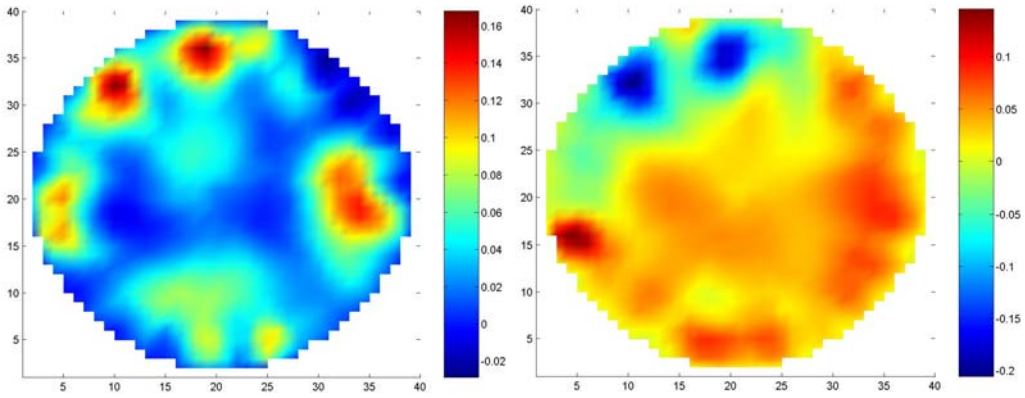

Figure 13. Panel A, amplitude map of 1st principal component (PC) of total Hb (82% of total variance). Panel B, amplitude map of 2nd PC of total Hb (10% of total variance).

5. Discussion

Central to the management of disease processes is an objective characterization of vascular hemodynamics. While it is understood that significant morbidity and mortality can result from focal disturbances in this parameter, mainly lacking has been the ability to explore such responses in large tissue structures using noninvasive imaging techniques. NIRS imaging, with its marked sensitivity to the hemoglobin signal, and availability of economical and portable instrumentation, we believe is an ideal technology to meet this need. Full development of this capability will require access to a comprehensive tool set that provides for, in addition to flexible strategies for data capture, capabilities that ensure data integrity, system reliability, image formation and enhancement, and signal analysis. Here we have outlined our approach to implementing these capabilities, and have presented results from preliminary clinical studies that support the contention that NIRS imaging holds the potential for broad-based assessment of focal hemodynamic disturbances. While evident, it is nevertheless deserves emphasis that these capabilities are achievable without the need of contrast agents or use of ionizing sources. Instead, image contrast obtained arises from the naturally occurring or induced variations in the light absorption properties of hemoglobin.

Motivating our development of the NIRS imaging technique to include the temporal dimension is appreciation that it can provide for a wealth of functional indicators that have previously stubbornly resisted systematic exploration using alternative imaging technologies. For instance, the results seen in response to transient induced hypoxemia of the breast are consistent with a longstanding notion that blood delivery to solid tumors is compromised by an underdeveloped vascular network. While this phenomenon is generally recognized, mainly absent are imaging tools capable of providing specific knowledge of the spatial extent and magnitude of this aberrant network. Information of this type could provide a basis for improved treatment planning (e.g., drug delivery, radiation therapy). We also recognize that light passing through tissue is encoded with information that is both temporally and spatially convolved. This argues for the use of signal separation techniques. We further recognize that the underlying connectivity of the vascular tree and its known modulation by local and systemic effectors suggests that simultaneous multi-site measurements could provide still additional sensitivity to the presence of subclinical disease processes and their characterization.

6. Acknowledgments

This work was made possible in part by support from the National Institutes of Health under Grants 5R21-HL67387-01 (SUNY), 1R21-DK63692 (SUNY), R43-CA91725-01-A1 (NIRx), and R41-CA96102

(NIRx); by the New York State Department of Health Empire Clinical Research Investigator Program (SUNY); by the US Army under Grant DAMD017-03-C-0018 (NIRx); and by the Stavros S. Niarchos Foundation (NYU).

7. References

[1] R. L. Barbour, J. Lubowsky, and H. L. Graber, "Use of reflectance spectrophotometry (RS) as a possible 3-dimensional (3D) spectroscopic imaging technique," *FASEB J.* **2**, A1772 (1988).

[2] R. L. Barbour, H. L. Graber, R. Aronson, and J. Lubowsky, "Model for 3-D optical imaging of tissue," *International Geoscience and Remote Sensing Symposium (IGARSS)* **2,** 1395-1399 (1990).

[3] R. Aronson, R. L. Barbour, J. Lubowsky, and H. L. Graber, "Application of transport theory to infra–red medical imaging," in *Operator Theory: Advances and Applications*, Vol. 51, pp. 64-75 (1991), Birkhauser Verlag Press (11th International Conference on Transport Theory, held in Blacksburg, VA, May 22-26, 1989).

[4] Proceedings of SPIE Vol. 4955 *Optical Tomography and Spectroscopy of Tissue V*, B. Chance, R. R. Alfano, B. J. Tromberg, M. Tamura, and E. M. Sevick-Muraca, Eds., SPIE Press, Bellingham, WA, 2003.

[5] Proceedings of SPIE Vol. 5138 *Photon Migration and Diffuse Light Imaging*, D. A. Boas, Ed., SPIE Press, Bellingham, WA, 2003.

[6] B. C. Wilson, M. S. Patterson, and S. T. Flock, "Indirect *versus* direct techniques for the measurement of the optical properties of tissues," *Photochemistry and Photobiology* **46**, 601-608 (1987).

[7] M. Cope and D. T. Delpy, "System for long-term measurement of cerebral blood and tissue oxygenation on newborn infants by near infra-red transillumination," *Medical and Biological Engineering and Computing* **26**, 289-294 (1988).

[8] B. W. Pogue, K. D. Paulsen, C. Abele, and H. Kaufman, "Calibration of near–infrared frequency–domain tissue spectroscopy for absolute absorption coefficient quantitation in neonatal head–simulating phantoms," *J. Biomedical Optics* **5**, 185-193 (2000).

[9] V. Ntziachristos and B. Chance, "Accuracy limits in the determination of absolute optical properties using time–resolved NIR spectroscopy," *Medical Physics* **28**, 1115–1124 (2001).

[10] R. L. Barbour, H. L. Graber, Y. Pei, S. Zhong, and C. H. Schmitz, "Optical tomographic imaging of dynamic features of dense-scattering media," *J. Opt. Soc. Am. A.* **18**, 3018-3036 (2001).

[11] Y. L. Pei, H. L. Graber, and R. L. Barbour, "Influence of systematic errors in reference states on image quality and on stability of derived information for DC optical imaging," *Applied Optics* **40**, 5755-5769 (2001).

[12] A. Y. Bluestone, G. Abdoulaev, C. H. Schmitz, R. L. Barbour, and A. H. Hielscher, "Three-dimensional optical tomography of hemodynamics in the human head," *Optics Express* **9**, 272-286 (2001).

[13] C. H. Schmitz, H. L. Graber, H. B. Luo, I. Arif, J. Hira, Y. L. Pei, A. Bluestone, S. Zhong, R. Andronica, I. Soller, N. Ramirez, S. L. S. Barbour, and R. L. Barbour, "Instrumentation and calibration protocol for imaging dynamic features in dense-scattering media by optical tomography," *Applied Optics* **39**, 6466-6486 (2000).

[14] C. H. Schmitz, M. Locker, J. M. Lasker, A. H. Hielscher, and R. L. Barbour, "Instrumentation for fast functional optical tomography," *Review of Scientific Instruments* **73**, 429-439 (2002).

[15] A. M. Siegel, J. J. A. Marota, and D. A. Boas, "Design and evaluation of a continuous–wave diffuse optical tomography system," *Optics Express* **4**, 287-298 (1999).

[16] D. A. Boas, T. Gaudette, and S. R. Arridge, "Simultaneous imaging and optode calibration with diffuse optical tomography," *Optics Express* **8**, 263-270 (2001).

[17] R. C. Collin, "The application of reciprocity and field equivalence principles to scattering from random media," in *Multiple Scattering of Waves in Random Media and Random Rough Surfaces*, V. V. Varadan and V. K. Varadan, Eds., pp. 119-138, Pennsylvania State University Press, University Park, PA (1985).

[18] Y. Pei, "Optical Tomographic Imaging Using Finite Element Method," Ph.D. Dissertation, Polytechnic University, Brooklyn, NY, 1999.

[19] K. D. Paulsen and H. Jiang, "Spatially varying optical property reconstruction using a finite element diffusion equation approximation," *Medical Physics* **22**, 691-701 (1995).

[20] A. H. Gandjbakhche, R. Nossal, and R. F. Bonner, "Resolution limits for optical transillumination of abnormalities deeply embedded in tissues," *Medical Physics* **21**, 185-191 (1994).

[21] H. L. Graber, Y. Xu, Y. Pei, and R. L. Barbour, "Spatial deconvolution technique for improving accuracy of reconstructed 3-D diffuse optical tomographic images," submitted.

[22] Y. Pei, H. L. Graber, Y. Xu, and R. L. Barbour, "*dyna*LYZE—a Matlab-based analysis package for dynamic optical tomography with the DYNOT system," 2004 OSA Biomedical Topical Meetings (Miami Beach, FL, Apr. 14-17 2004).

[23] F. Hlawatsch, G. Matz, H. Kirchauer, W. Kozek, "Time–frequency formulation, design, and implementation of time-varying optimal filters for signal estimation," *IEEE Transactions on Signal Processing* **48**, 1417-1432 (2000).

[24] M. Stetter, *Exploration of Cortical Function*, Kluwer Academic, Boston, (2002).

[25] H. L. Graber, Y. Pei, R. L. Barbour, D. K. Johnston, Y. Zheng, and J. E. Mayhew, "Signal source seperation and localization in the analysis of dynamic near-infrared optical tomographic time series," Proceedings of SPIE Vol. 4955: *Optical Tomography and Spectroscopy of Tissue V,* B. Chance, R. R. Alfano, B. J. Tromberg, M. Tamura, and E. M. Sevick-Muraca, Eds., pp. 31-51, SPIE Press, Bellingham, WA (2003).

[26] J. V. Stone, "Independent component analysis: an introduction," *Trends in Cognitive Science* **6**, 59-64 (2002).

[27] C. H. Schmitz, H. L. Graber, and R. L. Barbour, "Data integrity assessment and instrument calibration for the DYNOT imaging system," 2004 OSA Biomedical Topical Meetings (Miami Beach, FL, Apr. 14-17 2004).

[28] Y. Pei, H. L. Graber, and R. L. Barbour, "A fast reconstruction algorithm for implementation of time-series DC optical tomography," Proceedings of SPIE Vol. 4955: *Optical Tomography and Spectroscopy of Tissue V,* B. Chance, R. R. Alfano, B. J. Tromberg, M. Tamura, and E. M. Sevick-Muraca, Eds., pp. 236-245, SPIE Press, Bellingham, WA (2003).

[29] G. Strangman, J. P. Culver, J. H. Thompson, and D. A. Boas, "A quantitative comparison of simultaneous BOLD fMRI and NIRS recordings during functional brain activation," *Neuroimage* **17,** 719-731 (2002).

[30] R. B. Buxton, *Introduction to Functional Magnetic Resonance Imaging: Principles and Techniques*, Cambridge University Press, Cambridge, (2002).

[31] *Blood Perfusion and Microenvironment of Human Tumors*, M. Molls and P. Vaupels, Eds., Springer-Verlag, Berlin, 2000.

[32] G. S. Landis, T. F. Panetta, S. B. Blattman, H. L. Graber, Y. Pei, C. H. Schmitz, and R. L. Barbour, "Clinical applications of dynamic optical tomography in vascular disease," Proceedings of SPIE, Vol. 4250: *Optical Tomography and Spectroscopy of Tissue IV*, B. Chance, R. R. Alfano, B. J. Tromberg, M. Tamura, E. M. Sevick-Muraca, Eds., pp. 130-141 (2001).